A simple pendulum borehole tiltmeter based on a triaxial optical-fibre displacement sensor

P Chawah, J Chéry, F Boudin, Michel Cattoen, Han Cheng Seat, Guy Plantier, Françoise Lizion, A Sourice, Patrick Bernard, C Brunet, et al.

Paper accepted in
Geophysics Journal International (2015) **203**, 1026–1038 doi: 10.1093/gji/ggv358

A simple pendulum borehole tiltmeter based on a triaxial optical-fibre displacement sensor

P. Chawah,[1,2] J. Chéry,[1] F. Boudin,[1] M. Cattoen,[3,4] H.C. Seat,[3,4] G. Plantier,[2] F. Lizion,[3,4] A. Source,[2] P. Bernard,[5] C. Brunet,[5] D. Boyer[6] and S. Gaffet[6]

[1] *Géosciences Montpellier, CNRS-Université de Montpellier, France. E-mail: jchery@um2.fr*
[2] *ESEO, Angers and LAUM-Le Mans, France*
[3] *CNRS, LAAS, F-*31400 *Toulouse, France*
[4] *Univ de Toulouse, INP, LAAS, F-*31400 *Toulouse, France*
[5] *IPG, Paris, France*
[6] *LSBB, Rustrel, France*

SUMMARY

Sensitive instruments like strainmeters and tiltmeters are necessary for measuring slowly varying low amplitude Earth deformations. Nonetheless, laser and fibre interferometers are particularly suitable for interrogating such instruments due to their extreme precision and accuracy. In this paper, a practical design of a simple pendulum borehole tiltmeter based on laser fibre interferometric displacement sensors is presented. A prototype instrument has been constructed using welded borosilicate with a pendulum length of 0.85 m resulting in a main resonance frequency of 0.6 Hz. By implementing three coplanar extrinsic fibre Fabry-Perot interferometric probes and appropriate signal filtering, our instrument provides tilt measurements that are insensitive to parasitic deformations caused by temperature and pressure variations. This prototype has been installed in an underground facility (Rustrel, France) where results show accurate measurements of Earth strains derived from Earth and ocean tides, local hydrologic effects, as well as local and remote earthquakes. The large dynamic range and the high sensitivity of this tiltmeter render it an invaluable tool for numerous geophysical applications such as transient fault motion, volcanic strain and reservoir monitoring.

Key words: Tides and planetary waves; Transient deformation; Geomechanics.

1 INTRODUCTION

Earthquake precursory phenomena are part of a much broader class of unstable processes in the crust (Bernard 2001), such as slow earthquakes and episodic fault slips (Schwartz & Rokosk 2007). GPS-based instruments are able to measure only slow slips at depths that have large amplitudes while seismometers are insensitive to these low-frequency crustal strains. Recent studies aiming to understand these phenomena reveal a strong interest for analysing tilt signals (Hirose 2011). Although long-baseline strainmeters and tiltmeters provide the ultimate resolution and stability when installed at depths in tunnels, borehole tiltmeters are potentially competitive because they can be deployed as a network of sensors. However, a challenging aspect of borehole instruments remains their capability to concurrently display good resolution and small instrumental drift. In addition, short baseline instruments are sensitive to local effects (Agnew 1986). Since the tilt to be measured is in the nrad or μrad range, instruments like horizontal pendulums (Kato 1977) or folded pendulums (Wu *et al.* 2002) can artificially amplify the actual tilt amplitude. Nonetheless, horizontal pendulums are astatic (Skalsky & Picha 1969) and the small structure of the folded pendulums limits their coupling surface. A tiltmeter measures the variation of the orientation of the instrument body with respect to the local gravity vector. Therefore, a simple pendulum embedded into a borehole is well adapted for geophysical studies as demonstrated in many cases (Rosenbach & Jacoby 1969; Allen 1972; Allen *et al.* 1973; Sakata & Sato 1986; Jahr *et al.* 2006). These devices also allow for studying the surface strain associated with seasonal hydrological phenomena, seasonal behaviour or thermo-elastic underground processes (e.g. Weise *et al.* 1999; Kümpel *et al.* 2001). Most of the previously developed simple pendulums use capacitive sensors having excellent sensitivity. The recent improvement of field-deployable fibre interferometric optical displacement sensors (Chawah *et al.* 2012) in terms of robustness, precision and resolution offers a novel alternative in tiltmetry that is described here.

In this paper, a new experimental device is described. This optical borehole tiltmeter (OBT) consists of a simple pendulum tiltmeter incorporating three coplanar optical displacement sensors to measure the tilt of a swinging bob. The principal reason for exploiting optical measurements over bulb tiltmeters such as the Applied Geomechanics LILY, the Pinnacle Technologies 5000 or Askania capacitive-transducer tiltmeters (Weise *et al.* 1999) is to conceive

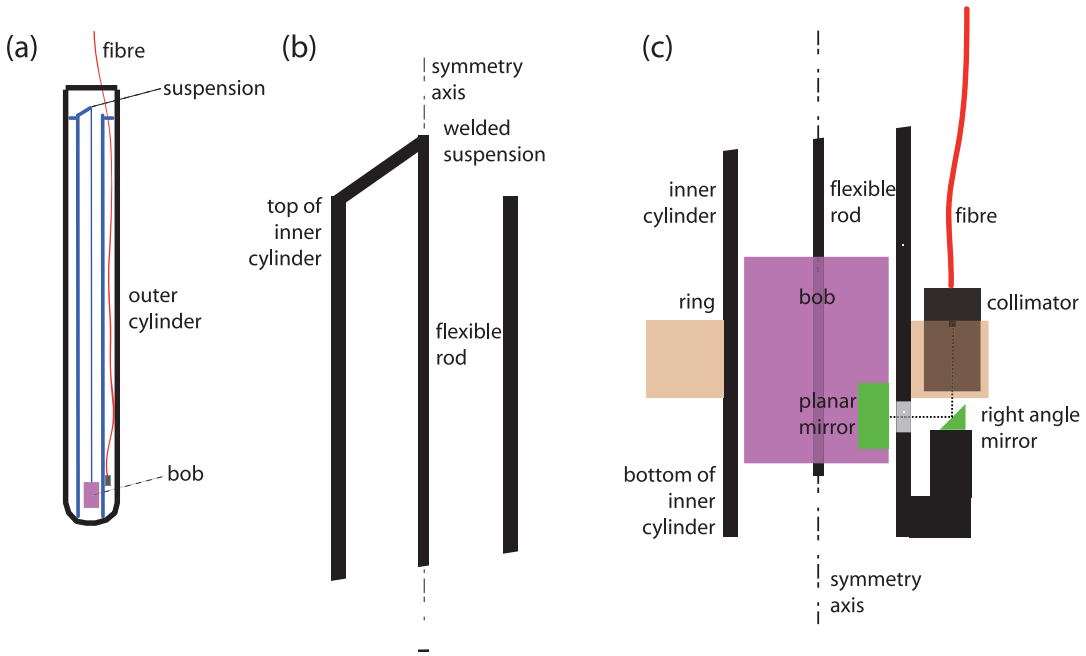

Figure 1. Optical borehole tiltmeter design. (a) general view of the instrument including outer and inner cylinders. Only one of the three fibres is shown; (b) closed-up of the upper part of the inner cylinder with the flexible rod suspension; (c) closed-up of bottom of the inner cylinder with the mobile bob and the components associated with the interferometer. Collimators are inserted in holes machined into the bronze ring. The three collimators, right angle mirrors and planar mirrors are disposed equilaterally at 120° as shown in Fig. 3.

a device free from electronics in the borehole. We thus employ three optical fibre interferometric probes from the extrinsic fibre Fabry-Perot interferometer (EFFPI) which intrinsically do not require any on-probe electronics (Seat *et al.* 2012). In addition, the tri-axial optical measurements can allow calculation of the bob's motion independent of temperature and pressure effects or from other common-mode perturbations.

In the context of the French ANR RiskNat-LINES project, a prototype of this instrument, denoted as LINES-OBT, has been deployed in the low-noise underground laboratory of Rustrel (LSBB-Rustrel) in southern France. We first detail the operating principles of the tiltmeter followed by a description on the integration of the EFFPI into the complete instrument. Finally, we demonstrate the calibration procedure of the instrument as well as illustrate its performance characteristics with the recording of Earth and Ocean tides, hydrological local effects and seismic activities.

2 PRINCIPLE AND DESIGN OF THE LINES-OBT

LINES-OBT consists of a main frame made of a borosilicate cylinder (Fig. 1). Inside this external cylinder, another borosilicate cylinder contains the pendulum itself and the three coplanar interferometric probes. Since the internal and external cylinders are rigidly coupled, the tilt of the internal frame varies identically to that of the external frame. The pendulum is made of a cylindrical bob attached to a thin rod (of 2 mm in diameter). The upper extremity of the rod is welded to the inner cylinder in order to avoid any spurious deformations. Both the frames and the rod are made of borosilicate and, hence, considered monolithic in order to minimize temperature effects (dilation coefficient of 3.3×10^{-6} K^{-1}). The measurement of the relative movement between the inner frame and the pendulum then allows the tilt variation of the structure to be determined. Contrary to other borehole tiltmeters (such as the Askania, Pinnacle and Applied Geomechanics instruments), our instrument does not incorporate a levelling system allowing the tilt sensor to be in vertical position. Indeed, it is considered difficult or almost impossible to suppress the mechanical drift associated with such a levelling system. Therefore, the pendulum (inner cylinder) is therefore rigidly clamped onto the external cylinder. The whole instrument (tiltmeter) is then hold into a vertical position with a precision of 0.5 mm m^{-1} and finally backed by surrounding silica beads. This enables the pendulum frame to be directly coupled to the surrounding rock, which is mandatory for keeping its instrumental drift as low as possible.

A simple pendulum can be described using a model in which a bob is suspended from a pivot at the extremity of a rod (Fig. 2). When studying the 3-D movements of the bob due to a mobile rod in an inertial space, five variables can be used to describe the five degrees of freedom of the system (three linear coordinates related to the pivot's displacement and two angular coordinates relative to the bob's swing). However, we limit our study of the bob's movement to a vertical 2-D plane in a Cartesian coordinate system. When a sudden or continuous frame tilt occurs, the pendulum reacts by oscillating. Since P is a flexible hinge, a slight flexure is then induced in the rod. When the frame undergoes a very slow or quasi-static tilt of angle $\Lambda(t)$, the bob then naturally repositions itself in order to maintain its equilibrium close to the local vertical (Fig. 2). After a sudden tilt or translation, we observe that the bob's motion typically settles into a steady state after 120 s. This damping is principally due to the friction between the bob and the air within the inner cylinder.

We use the Lagrangian formulation for a non-conservative system to describe its equilibrium. This technical development, detailed in Appendix A, leads to the formulation of a damped harmonic oscillator responding to the tilt $\Lambda(t)$ and translation $X_P(t)$ of the frame since both are interdependent.

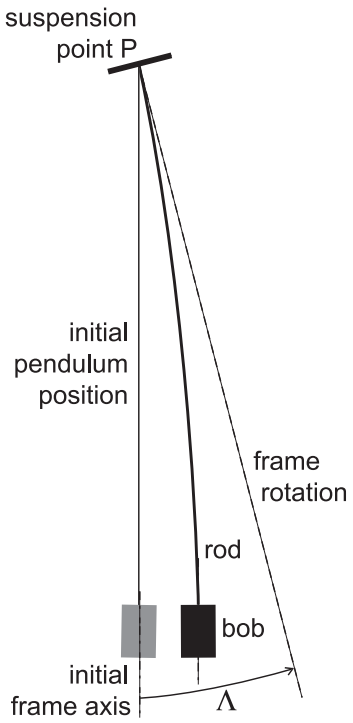

Figure 2. Representation of the pendulum when the bob is moving due to a rotation Λ of the referential (P, x, y, z). Note that motion and rotation are largely magnified. Real geophysical rotations are of the order of 1 µrad.

Using appropriate values of the geometrical parameters of the pendulum together with those of the mechanical parameters (Table 1), we determine its theoretical oscillation frequency to be ∼0.585 Hz.

3 MEASUREMENT OF THE BOB'S MOVEMENT: THE OPTICAL TRI-AXIAL DISPLACEMENT SENSOR

The relative motion of the bob with respect to the pendulum frame induced by natural vibration and rotation is limited to 1 mm by construction while typical amplitudes due to natural ground vibration are generally lower than 10 µm. Hence, for a pendulum length of ∼0.86 m, the displacement of the bob at the end of the pendulum is therefore practically planar. The tracking of this movement is ensured by three optical measurements in a horizontal plane as shown in Fig. 3. The principal motivation of employing three-axis displacement measurements $[d_1(t), d_2(t), d_3(t)]$ in a 2-D Cartesian

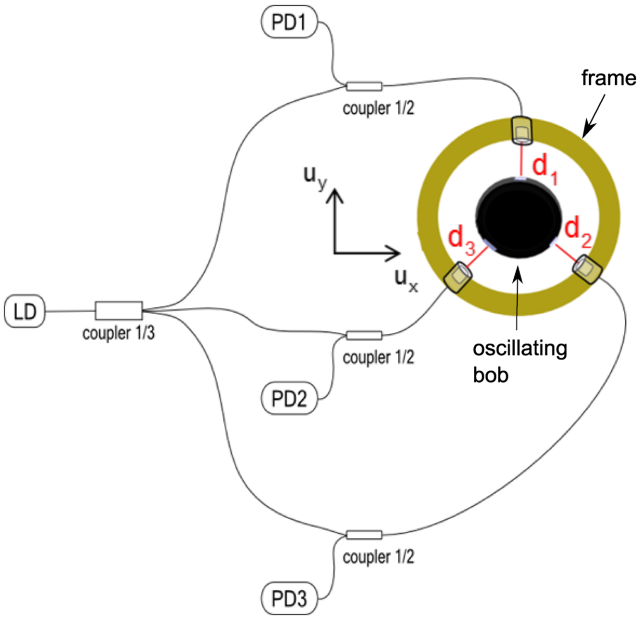

Figure 3. Schematic showing the tiltmeter's coplanar displacement sensor. A single laser diode (LD) illuminates three fibre optical circuits connected to the three collimators held in a bronze ring as illustrated by Fig. 1. (PD1, 2 and 3 represent photodetectors 1, 2 and 3)

coordinate system ($\vec{u_x}$ and $\vec{u_y}$) is to obtain an overdetermined system so that differential measurements can be performed. Since the three displacement sensors are positioned in a manner symmetrical with respect to the pendulum's symmetry axis, the three optical measurements are identically affected by physical phenomena such as temperature, pressure or air refractive index variation. The displacement variations, common to all the optical axes (referred to here as common-mode), can also result from a variation of the optical wavelength of the single laser diode used in the optical circuit shown in Fig. 3. Subsequently, these variations correspond to the same apparent movement $\bar{d}(t)$, as 'seen' by the three measurement axes. Each optical axis is a Fabry-Perot cavity consisting of a collimated laser probe beam pointing at a mirror glued to the oscillating bob. In the current system, the three optical axes intersect at the centre of the bob, forming an angle of 120° between each adjacent axis. In this configuration, displacements d_1, d_2 and d_3 are thus considered positive as the distance between the corresponding optical probe and the mirror increases (in other words when the distance variation is positive). Thus, with the three interdependent optical measurements, we are able to estimate the Cartesian

Table 1. Geometrical and mechanical properties of the tiltmeter. Errors are expected to be lower than 2 per cent. However, rod's diameter is known at a precision of 10 per cent only.

Symbol	Meaning and unit	Value
M	Mass of the rod and bob (kg)	0.207
E	Young's modulus of the rod (GPa)	69
D	Diameter of the rod (m)	0.002
J_G	Quadratic moment (m^4)	1.15×10^{-12}
L	Length of the rod (m)	0.85
R	Radius of gyration (m)	0.84
l	Distance from the rotation centre P to the pendulum's inertial centre (m)	0.83
L_e	Equivalent pendulum length (m)	0.70
ξ	Damping ratio	0.02
Ω_1	Ideal natural angular frequency (rad s^{-1})	3.4
Ω_0	Theoretical angular frequency (rad s^{-1})	3.68

components of the movement free from common-mode disturbances. This characteristic is described in the next paragraph.

Let $d_1'(t)$, $d_2'(t)$ and $d_3'(t)$ be the reduced measurement of $d_1(t)$, $d_2(t)$ and $d_3(t)$ corresponding to what would be directly measured in an ideal case for which the unknown common-mode $\bar{d}(t)$ is equal to zero. Hence, they represent the images of the ideal displacements on the three axes and can be written as:

$$d_i'(t) = d_i(t) - \bar{d}(t), \quad i = 1, 2, 3. \tag{1}$$

In order to facilitate the calculus, we chose to orientate the unit vector $\overrightarrow{u_y}$ parallel to the d_1 axis, as shown in Fig. 3. We then deduce the relationships between the measured displacements along their axis and the displacement on the OX–OY Cartesian plane:

$$\begin{aligned} d_1'(t) &= d_1(t) - \bar{d}(t) = -u_y(t) \\ d_2'(t) &= d_2(t) - \bar{d}(t) = -u_x(t)\cos\frac{\pi}{6} + u_y(t)\sin\frac{\pi}{6} \\ d_3'(t) &= d_3(t) - \bar{d}(t) = u_x(t)\cos\frac{\pi}{6} + u_y(t)\sin\frac{\pi}{6}. \end{aligned} \tag{2}$$

The sum of eq. (2) leads to a simple value of $\bar{d}(t)$ which is equal to $\frac{1}{3}[d_1(t) + d_2(t) + d_3(t)]$. Three expressions can be written to determine the $u_x(t)$ component:

$$\begin{aligned} u_x(t) &= -\frac{\left[d_2(t) - \bar{d}(t)\right] + \left[d_1(t) - \bar{d}(t)\right]\sin\pi/6}{\cos\pi/6} \\ u_x(t) &= \frac{\left[d_3(t) - \bar{d}(t)\right] + \left[d_1(t) - \bar{d}(t)\right]\sin\pi/6}{\cos\pi/6} \\ u_x(t) &= \frac{d_3(t) - d_2(t)}{2\cos\pi/6} \end{aligned} \tag{3}$$

and subsequently, the $u_y(t)$ component can be expressed in two ways :

$$\begin{aligned} u_y(t) &= -\left[d_1(t) - \bar{d}(t)\right] \\ u_y(t) &= d_2(t) + d_3(t) - 2\bar{d}(t). \end{aligned} \tag{4}$$

In practice, we notice that the common-mode evolves slowly with time, most probably due to the slow evolution of the laser diode wavelength, temperature, pressure and air refractive index. We therefore evaluate the common mode $\bar{d}(t)$ by averaging it on a 0.1–1 s time range and invert the linear system of eq. (4) to provide u_x and u_y at a 250 Hz sampling rate. In this way, the bob's motion and the tilt free from both optical and thermomechanical variations can be obtained. However, this technique does not account for minor structural asymmetry that may occur when positioning the mirrors onto the bob, inducing angles that are slightly different from the ideal 120° (in the order of a tenth of a degree). Further, the optical axis may be slightly non-coplanar. In such a case, this angular asymmetry can be taken into account in eq. (2) and the determination of these angles is detailed in Chawah (2012) and Chéry & Collard (2013).

4 THE EXTRINSIC FIBRE FABRY-PÉROT INTERFEROMETER (EFFPI)

The tracking of the coplanar displacements of the oscillating bob is achieved by three EFFPI sensor probes that are illuminated by a single laser diode (LD) source as schematically illustrated in Fig. 4. The operating principles of the EFFPI and the techniques used for the acquisition and signal processing schemes are detailed in Chawah *et al.* (2012) and Seat *et al.* (2012), hence, only the major characteristics of the sensor shall be mentioned in this paper.

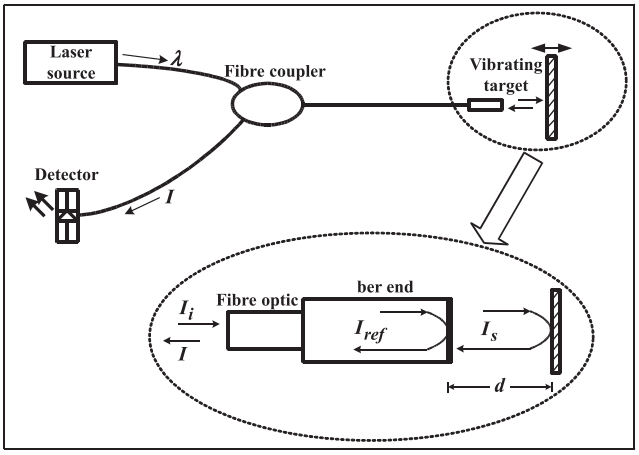

Figure 4. The extrinsic fibre Fabry-Perot interferometer. The main beam I_i splits at the fibre end, creating the reference beam I_{ref} and the sensing beam I_s. The recombined beams forming the interference signal is noted as I.

The EFFPI is a fibre interferometric sensor capable of detecting displacements of a moving or immobile element down to the nanometric order. The sensing cavity represented in Fig. 4 is formed by the cleaved end of an optical fibre and the surface of a displacement element, which is a mirror here. The displacement to be measured $d(t)$ represents the path difference traversed by the sensing beam with respect to the reference beam. The difference between the EFFPI and other fibre interferometers (such as the Michelson or Mach–Zehnder devices) lies in both the reference and the sensing beams propagating along a common path in the same fibre. The reference beam is back-reflected at the fibre–air interface (∼4 per cent of injected LD emission) while the remaining beam is transmitted through this interface to a sensing cavity before being reflected by the mirror along the same optical path. A photodetector is then used to detect the interference signal resulting from the superposition of the reference and sensing waves at the fibre end. Subsequently, the displacement $d(t)$ is recovered by estimating the phase of the detected interference signal $S(t)$ via:

$$\varphi(t) = 4\pi n\frac{d(t)}{\lambda_0}, \tag{5}$$

where n is the refractive index of the cavity and $\lambda_0 = 1310$ nm is the emitted wavelength from the LD. Further, the fundamental optical effect of positioning the fibre end at the focal plane of the collimator together with the use of a high-reflectivity target mirror enables a second reflection in the optical cavity to be achieved. This double reflection enables the sensor's resolution to be doubled and, more importantly, allows the alignment tolerance to be relaxed to better than ±0.5° along the optical axis. In this way, one complete interference fringe will represent a displacement amplitude of λ/4. Nevertheless, in order to completely describe the displacement in terms of its amplitude as well as it directional movement, having only $\varphi(t)$ is not sufficient. Hence, as described in Seat (2012) and Chawah (2012), by modulating the LD current, we are able to extract two phase-quadrature signals $V_x(t)$ and $V_y(t)$ from $\varphi(t)$ in a Cartesian plane such that

$$\begin{aligned} V_x(t) &= V_{0_x} + V_{m_x}\cos(\varphi(t) + \alpha) \\ V_y(t) &= V_{0_y} + V_{m_y}\sin\varphi(t), \end{aligned} \tag{6}$$

where $V_x(t)$ plotted against $V_y(t)$ represents an elliptic Lissajous trace with V_{0_x} and V_{0_y} the coordinates of the ellipse's centre, V_{m_x} and V_{m_y} the primary and secondary axis lengths, and α the

orientation of the primary and secondary axes on the Cartesian plane. These parameters are quasi-stable and may vary slowly over time due to temperature variations or other parasitic perturbations. Further, when the object is immobile or displaces very slowly, then no fringes are formed and the Lissajous trace exhibits just a single point. No displacement demodulation is then possible. This behaviour is overcome by employing a second modulation to the LD current to generate an additive virtual or reference displacement.

Two methods are used to process the signals in quadrature, as mentioned in eq. (5), in order to extract the phase term $\varphi(t)$. The first method consists of geometrically estimating and updating the ellipse parameters at the beginning and end of each recording (Seat *et al.* 2012). This phase demodulation method is technically equivalent to the quadrature error correction and compensation technique reported by Zumberge *et al.* (2004) as well as similar to that proposed by Pozar & Mozina (2011), both of which are derived from the technique initially demonstrated by Heydemann (1981). However, the LD modulation scheme employed in this work to obtain the quadrature signal pair enables quasi-static or static movements with a precision better than 2 nm over a large bandwidth to be detected, a significant advantage when observing crustal behaviour. Zumberge's technique can potentially allow such movements to be measured but the correction scheme proposed by Pozar and Mozina has typically been used only for periodically displacing targets. A second quadrature signal processing method has also been implemented (Chawah *et al.* 2012). Here, the necessary ellipse parameters are calculated and updated in real time at each acquisition of a new $V_x(t)$, $V_y(t)$ pair using an adaptive Kalman filter. This allows eliminating the amplitude modulation in the quadrature signals caused by the current modulation along with any temperature and pressure effects on the laser diode level.

After estimating the ellipse parameters, a normalization of eq. (6) is then carried out. Finally, $\varphi(t)$ can be calculated by applying the arctan function to the normalized interference signals from which the displacement, $d(t)$, is subsequently demodulated. The EFFPI sensor has been calibrated over a 2–5000 nm displacement range with a reference piezo-electric transducer, resulting in a 2 nm precision and a resolution in the pm range over a bandwidth of 10^{-3} to 500 Hz. The modulation-based EFFPI device currently has a patent application pending (Cattoen & Seat 2012).

5 TILTMETER CALIBRATION AND PRELIMINARY EXPERIMENTAL RESULTS

To calibrate the complete instrument and verify the effectiveness of the tri-axial measurements, the tiltmeter is mounted onto a tripod as shown in Fig. 5. The set-up is then excited under forced-state conditions by a piezoelectric plate placed under one of the tripod legs. A Heaviside excitation is next employed to stimulate all the natural frequencies of the tiltmeter. As demonstrated by the Fourier transform of the measured displacement $d_1(t)$ in Fig. 6, a frequency peak is observed at 0.6 Hz (or 1.66 s), very close to the theoretical natural frequency of 0.585 Hz of the pendulum. Also, we experimentally obtain a value of 0.02 for the damping factor ξ. The Fourier transform indicates that the pendulum's natural oscillation is not the unique movement mode experimentally observed. Indeed, a transverse vibration of the borosilicate rod has also been experimentally detected. Thus, when the structure undergoes an external excitation, the hinge P (visible in Fig. 2) transmits a mechanical wave that propagates through the rod. This movement is illustrated

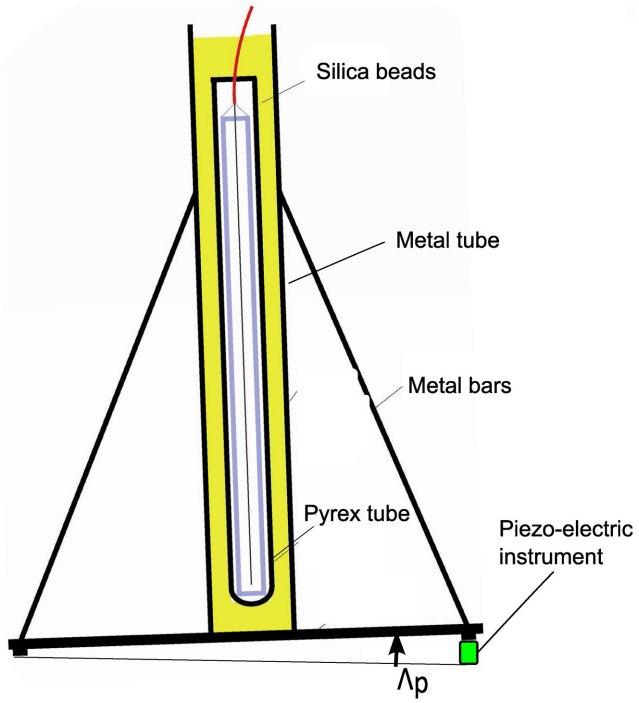

Figure 5. Front view of the tripod holding LINES-OBT. Silica beads ensure coupling between the tripod and the tiltmeter. Vertical motion of the piezo-electric transducer located beneath one tripod leg provides frame rotation around a horizontal axis formed by the two other tripod legs.

in Fig. 6 by the two frequency peaks at 12 and 26 Hz. These peaks may represent the modes of the suspended rod's vibration. On the other hand, the resonance of the tripod itself may also introduce additional vibration modes to the instrument's frequency spectrum. The other frequency bands present in the spectrum have been investigated and are attributed to oscillations due to ventilation noises in the laboratory. In order to investigate whether or not the 12 and 26 Hz are tied to the rod's pendulum vibration, we compute the resonant modes of the rod following the mechanical approach of Blevins (2001). We first consider that the rod has no rigidity and is submitted to bob's tension. For this case, the two first resonant frequencies are 9.08 and 18.16 Hz. We must acknowledge that the rod's diameter is known at 10 per cent accuracy that may significantly affects the computed frequencies. However, we remark that successive values have a ratio of 2.00, markedly different from the observed ratio of 2.16. We then consider elastic rod's properties, assuming a rigid hinge and a vertical load due to bob's tension (Blevins 2001). In this case, the two first frequencies are 12.98 and 32.33 Hz, still different from observed values. The frequency ratio of 2.49 is larger than the observed value. Due to the relatively good agreement between observed and computed frequencies, we conclude that resonant peaks of 12 and 26 Hz are likely linked to transverse rod motion triggered by ambient vibrations.

The analysis mentioned in the previous paragraph also enables us to calibrate the static behaviour of the pendulum. The piezoelectric plate is positioned at a distance of 0.72 m from the rotation axis with respect to the two other legs. A sinusoidal vertical excitation with a peak-to-peak amplitude of 13.5 μm is next applied to the tripod's leg to generate a rotation of the pendulum frame tilt of 18.75 μrad. The horizontal displacement of the bob with respect to the tiltmeter frame during the oscillations is measured using the three interferometric probes. The tiltmeter frame tube is then rotated by 10° steps around its vertical axis and the displacement

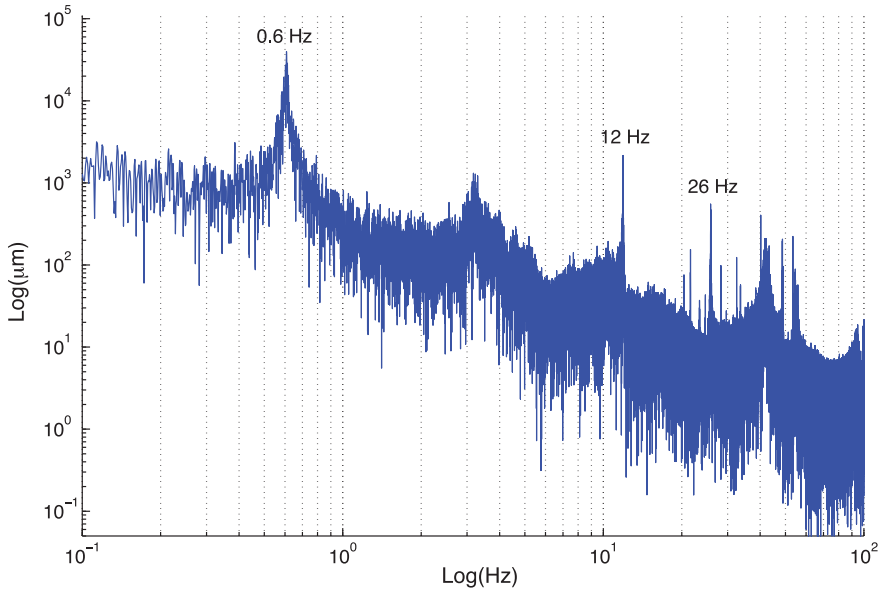

Figure 6. Resultant Fourier transform of $d_1(t)$ after a square excitation of the tiltmeter by the piezo-electric plate. The 0.6 Hz frequency band denotes the fundamental oscillating mode whereas the 12 Hz and the 26 Hz bands indicate the rod's vibration modes. The remaining frequency bands are likely to be caused by parasitic movements in the laboratory.

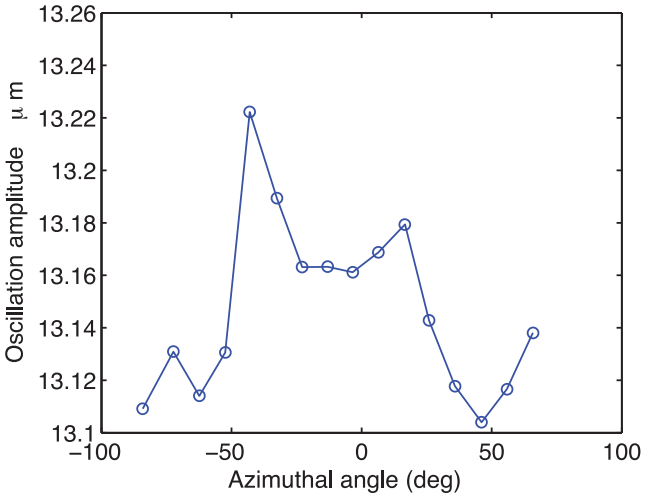

Figure 7. The amplitude of the sinusoidal component of the pendulum oscillations as a function of azimuthal angle (clockwise from north). The forced oscillation of the tripod is induced using a piezoelectric plate. The observed variation could be due to angles of eq. (4) being slightly different from $\pi/6$.

measurement repeated. These displacements are post-processed to eliminate the resonance from the natural frequency as follows. A virtual damping precisely at the resonant frequency of the pendulum is introduced using the approach originally proposed by Wiener (1949). The Wiener–Hopf equations are next used to calculate the coefficients of the impulse response of an equalizer filter, which, when convoluted with the pendulum response, result in a desired pattern (see Appendix B). The output of the equalizer filter then represents the movement of the equalized pendulum without resonance which enables the true sinusoidal component of the movement to be finally obtained using the least squares method. The symmetry illustrated in Fig. 7 indicates a quasi-isotropic behaviour. The pendulum displays a peak-to-peak motion ranging from 13.10 to 13.22 µm due to the applied tilt (18.75 µrad) of the frame. Therefore, the equivalent length L_e of a simple pendulum can be calculated experimentally by dividing the displacement u by the frame tilt Λ, to give 0.70 m with a 1 per cent uncertainty. Due to the rod's elasticity, L_e is ∼18 per cent shorter than the real pendulum length of 0.86 m. It is to be noted that this mechanical analysis does not account for other modes corresponding to the flexible rod's torsion and the bob's rotation around the pendulum's vertical axis. Although these motions are probably weak due to the system's symmetry, a complete mechanical and optical model of the pendulum should allow for detecting and, hence, correcting them.

6 INSTALLATION OF THE TILTMETER IN THE LSBB LABORATORY

Our measurement site is located in Rustrel, near the city of Apt (Vaucluse, France) in an underground low-noise laboratory (LSBB – http://www.lsbb.eu; Fig. 8a), located 70 km north of the Mediterranean Sea and 550 km east of the Atlantic Ocean. This facility includes a very long tunnel of ∼3000 m in which air circulation is controlled by airlocks. The tunnel is under a 500-m-thick rock layer made of karstified limestone thus ensuring an efficient thermal blanketing that maintains temperature variations to less than 0.1 °C. In addition, power spectrum analyses of seismic excitations in this facility reveal a low-noise environment (Gaffet *et al.* 2003). This site should therefore provide valuable environmental conditions for strain and tilt measurements. The tiltmeter (LINES-OBT) is installed at the end of the LINES gallery (Fig. 8b) which is separated from the main tunnel by two doors. This limits air circulation and therefore minimizes temperature variations inside the gallery. However, the doors are not airtight and hence do not induce the forming of pressure gradients. This gallery also hosts other geophysical instruments such as a hydrostatic long baseline tiltmeter of 150 m in length (whose axis is located 5 m away from the borehole of LINES-OBT) and a mono-axial seismometer (located 3 m away from LINES-OBT). These instruments are equipped with fibre optical interferometers identical to those integrated into the LINES-OBT. At approximately 2 m from LINES-OBT, another

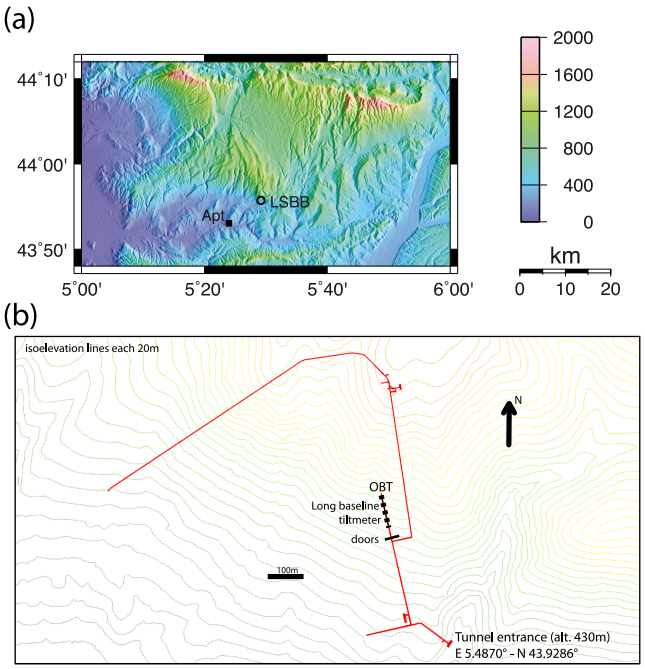

Figure 8. (a) LSBB laboratory location on the southern slope of Vaucluse plateau; (b) topography of the tunnel with galleries drawn in red. Tiltmeters are located in a N350 gallery closed by doors.

borehole tiltmeter (Applied Geomechanics LILY) is also installed for comparison.

The instruments are actually housed in a room at a depth of 300 m below the rock layer. In order to investigate the capability of remote measurements using long optical fibres as well as to isolate any electronic devices and human presence, the instruments were placed at approximately 250 m away from the laser sources, the photodiodes and the control computers. Two boreholes with a 12 cm diameter and 140 cm depth were drilled vertically into the ground to accommodate both LINES-OBT and LILY. During the installation phase in LSBB, we coupled both LILY and LINES-OBT to the ground using 1.5 mm diameter silica beads. This instrument-ground coupling is a very important factor for the measurement of the true ground tilt variation. Using packed granular materials such as clean quartz sand has been a standard method of emplacing tiltmeters in shallow boreholes since the 1970s (Allen *et al.* 1973; Mortensen & Johnson 1975; Wyatt & Berger 1980; Wyatt *et al.* 1988). However, since sand can deform due to grain rotation, spherical quartz beads are used here instead. This coupling mode has the advantage of providing a self-organized, stable and incompressible tetrahedral network of balls to enable a very stable configuration over time. Further, this technique can allow easy recovery of the instruments from the borehole since no irreversible chemical reaction takes place. Tiltmeter sealing was made in three steps. First, the bottom hole was filled by beads over a thickness of about 10 cm. Secondly, the tiltmeter was hold vertically at borehole centre and we ensured that the d_1 axis of the instrument was oriented northward using a compass, with a precision estimated to be $\sim$2–5° since the surrounding rock is entirely calcareous and contains almost no magnetic minerals. At this stage, we manually levelled the pendulum into vertical position with a precision of 0.05° using a small commercial tiltmeter attached to its frame. Finally, we filled the borehole by beads to ensure tiltmeter clamping over its full length. Tilt record started a few hours following this last operation.

LINES-OBT has been in continuous operation since March 2012 and the three displacement measurements recorded at a frequency of 250 Hz. The rare interruptions that occurred to the acquisition system were due to power cut-off within the LSBB facility. For example, during the first 4 months of operation, there were only two disruptions. Nevertheless, the control computer driving the acquisition and processing software can be accessed remotely via the Internet, and the entire system can be conveniently reactivated. In order to correlate the measured tilts with other physical parameters, we have also deployed three SENSIRION-SHT1x sensors, each measuring the temperature, atmospheric pressure, relative humidity and CO_2 concentration at 1 Hz in three different parts of the installation.

7 GEOPHYSICAL USE OF THE TILTMETER: HYDROLOGY AND EARTH TIDES

Despite the tiltmeter has been operating for more than 1 yr, only 6 months of continuously recorded data are available. Fig. 9 shows 4 months of displacement data filtered by a low-pass Butterworth filter and undersampled to achieve a reduced sampling period of 100 s. Slight gaps in the data were also corrected in this figure. Two components dominate the common-mode $\bar{d}$, namely, a slow variation of 2.3 μm over the entire period (Fig. 9b) and a small amplitude short-term component. To represent the latter, we fitted a third degree polynomial to $\bar{d}(t)$ which is then extracted for interpretation. An obvious correlation can be observed between the short-term component of $\bar{d}$ and the atmospheric pressure variation near the borehole tiltmeter (Figs 9c and d), with a coefficient of 6.1 nm hPa^{-1}. Pressure change is expected to alter the measured displacements d_1, d_2 and d_3 in two ways. First, a pressure increase in the tunnel is expected to occur in the borehole that is not sealed. Therefore, this should lead to an isotropic contraction of the outer cylinder of LINES-OBT. Because the outer cylinder and the tiltmeter are elastically coupled, the measured distances should therefore decrease. However, $\bar{d}$ and the atmospheric pressure are positively correlated, showing that the mechanical pressure effect does not explain the observed behaviour. Alternatively, the change of $\bar{d}$ could be caused by the slight variation of the optical refraction index with respect to the atmospheric pressure and the humidity variations. Using the formula proposed by Ciddor (1996) and at a wavelength of 1310 nm, we compute a wavelength change of -0.000347 nm hPa^{-1}, corresponding to a relative wavelength change of -2.65×10^{-7} hPa^{-1}. Since the Fabry-Perot cavity is 25 mm long, the expected apparent measured displacement $\bar{d}$ should be 6.625 nm hPa^{-1}. This is only slightly larger than the measured value of 6.1 nm hPa^{-1}. It is therefore probable that the refractive index variation is the main cause of the observed correlation between the common-mode displacement and atmospheric pressure.

Nevertheless, as has been explained previously, the Cartesian components of the movement $u_x(t)$ and $u_y(t)$ are independent of these perturbations. At low frequency, frame tilts, Λ_x in the east–west directions and Λ_y in the north–south direction can be calculated by dividing, respectively east–west displacement, $\overrightarrow{u_x}$, and south–north displacement, $\overrightarrow{u_y}$, by the equivalent length $L_e = 0.70$ m obtained during laboratory calibration. We first compared uncorrected tilts of the borehole tiltmeter with the long baseline tiltmeter installed in the same gallery at N350 azimuth (Fig. 10a). Due to its long baseline of 150 m, the latter instrument displays virtually no drift during its three first months of recording. By contrast,

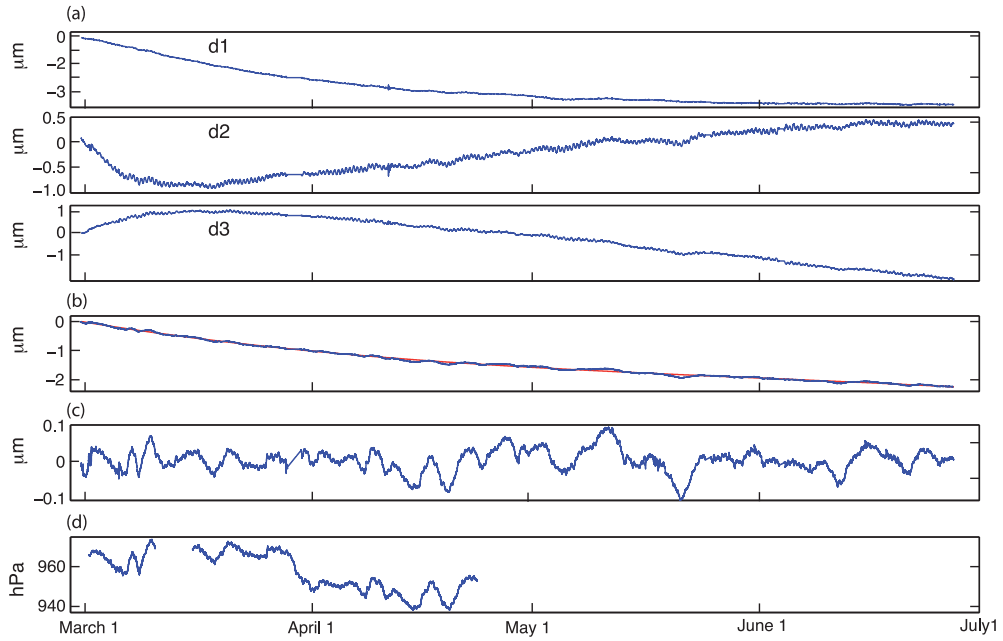

Figure 9. (a) Measured displacements $d_1(t)$, $d_2(t)$ and $d_3(t)$ from LINES-OBT during the four first months of recording. A record gap occurred around April 10th; (b) common-mode (in blue) and the third-order polynomial fitting of the common-mode (in red); (c) residual common-mode after trend removing; (d) atmospheric pressure measured in the LINES gallery.

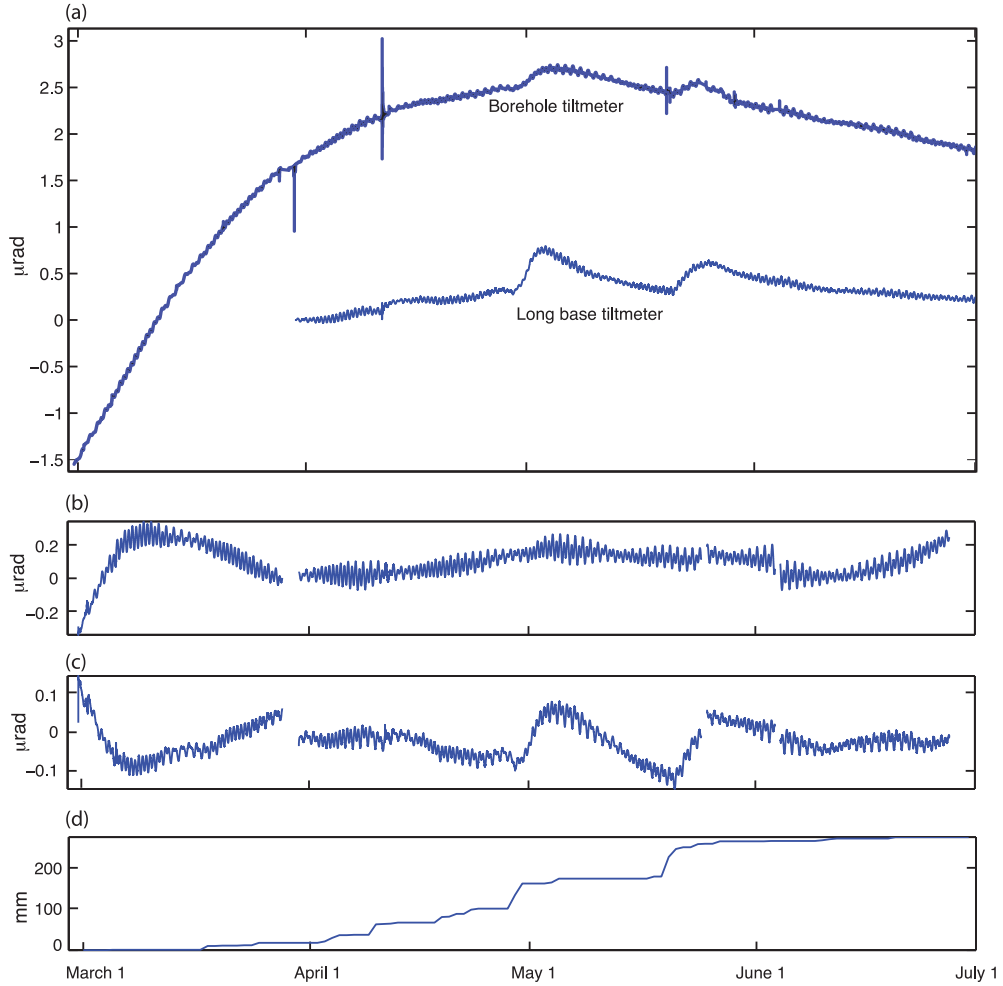

Figure 10. (a) Uncorrected tilt of borehole tiltmeter (LINES-OBT) and long baseline tiltmeter along N350 azimuth. Jumps associated with missing data are not corrected; (b) east–west tilt in µrad free from slow drifts (fourth-order polynomial fitting); (c) north–south tilt in µrad free from slow drifts; (d) cumulated sum of rainfall precipitations on a surface rain gauge.

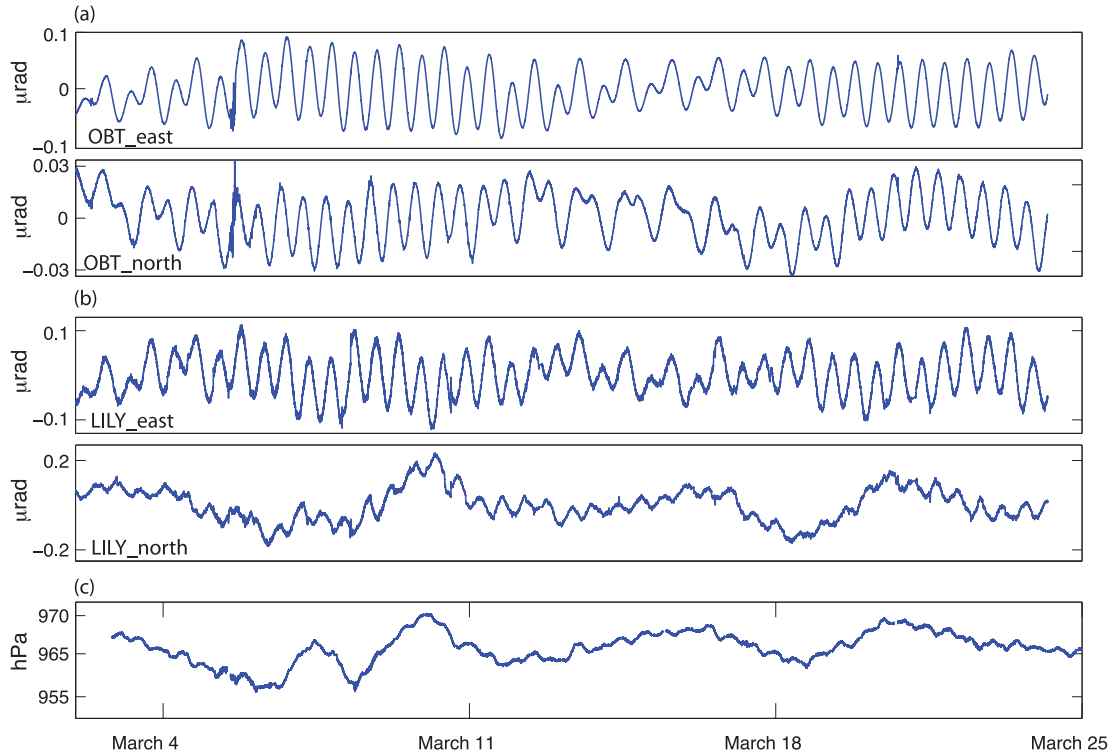

Figure 11. (a) Tilts in east–west and north–south axes, respectively calculated from the displacement components u_x and u_y; (b) tilts in µrad measured by the LILY tiltmeter along the same directions; (c) atmospheric pressure measured at the tunnel entrance.

LINES-OBT displays a linear drift of 0.25 µrad month^{-1} over a 2-month period (May–June). The comparison of the tiltmeter displacement measurements in the south–north direction free from the slow drift (Fig. 10c) and the rainfall precipitations (Fig. 10d) reveals a correlation between these two quantities. For instance, an initial strong tilt of 0.14 µrad observed on 2012, April 29th closely follows a 33 mm precipitation. Further, hydrological tilts measured by the long baseline tiltmeter are two times larger than those detected by LINES-OBT. We suspect local hydrological effects to be responsible for this discrepancy.

To better assess the tiltmeter performance, we pre-installed (in January 2012) an Applied Geomechanics LILY tiltmeter in a borehole situated at 1.5 m from LINES-OBT in order to compare the observations and the performances of the two instruments. Unfortunately, a power supply incident occurred to LILY (breakdown of the battery charger) on 2012 March 24 and an abnormal behaviour started appearing in its y-tilt component in April. However, both instrument are corrected for slow drift. Nonetheless, LINES-OBT data (Fig. 11a) correlate well with the E–W component of LILY (Fig. 11b). By contrast, both instruments do not compare well for the N–S component. The comparison between the N–S tilt measured by LILY and atmospheric pressure record (Fig. 11c) shows that atmospheric fluctuations have a clear impact on the recorded tilts by the LILY tiltmeter. The E–W component of LILY, on the other hand, seems not to be affected by pressure variations.

Apart from strong hydrological events, most of the daily tilt signal is associated with Earth tides. To evaluate how theoretical tides compare to LINES-OBT data, we compute E–W and N–S Earth tides using the ETERNA software (Wenzel 1996) over the first 4 months of recording. We also compute the contribution associated to oceanic tides (Boy *et al.* 2009). We estimate the phases and amplitudes on some frequency bands due to Earth tide modes (Table 2). The phase of the modelled tides match well with those of observed tides for the main semi-diurnal wave M_2. For this wave, we observed amplitudes of 49.3 and 14.8 nrad in the respective E–W and N–S directions. The corresponding amplitude factors between the observed and theoretical signals are 1.276 and 0.551 for the respective E–W and N–S directions. Further, the direct comparison between the observed and theoretical time series shows that E–W M_2 tides are larger than model prediction (Fig. 12a), while the observed N–S M_2 tides are much smaller than the theoretical tides (Fig. 12b). In addition, the ratio of the diurnal to semidiurnal tides for this component differs from the prediction as seen by the differing modulation. The smaller amplitudes of the observed N–S tides with respect to the prediction theory have previously been reported (e.g. King & Bilham 1973). This large discrepancy between the observed and modelled tides for the N–S component can be attributed to local effects which can be explained as follows. First, LINES-OBT is very close to the tunnel that may induce severe local strain disturbances (e.g. Harrison 1976). It has been reported that tidal tilts are strongly dependent on borehole configuration (Kohl & Levine 1995). Also, the LSBB tunnel is located on the southern slope of the Vaucluse plateau that displays a N–S slope of approximately 20° over 5 km. Such a steep topography may induce significant tide decrease as suggested by the theoretical study of Meertens & Wahr (1986). Finally, we estimate the noise level of LINES-OBT by computing its power spectral density (PSD) using the Welch's method (Welch 1967) over the first 4 months of recording (Fig. 13). As shown previously, diurnal and semi-diurnal tides components are largely above the noise level of the tiltmeter signal. However, LINES-OBT does not reveal the less energetic ter- and quarter-diurnal tides. Further quantification of LINES-OBT performance will require comparative analyses with other borehole and long baseline tiltmeters.

Table 2. Tides analysis processed using ETERNA software using a 4-month data set. Column 1: wave name; column 2: direction; column 3: observed amplitude; column 4: theoretical amplitude; column 5: ratio between theoretical and observed amplitude; column 6: rms (amplitude); column 7: phase shift between observed and theoretical phase; column 8: rms (phase).

Wave	Dir	Ampl. (obs) [nrad]	Ampl. (theor) [nrad]	Ratio	Stdv [nrad]	Ph. Lead [°]	Stdv. [°]
M2	EW	49.3	38.6346	1.2760	0.05	−9.2434	0.0690
	NS	14.8	26.85	0.551	0.007	0.7619	0.2062
O1	EW	14.4	15.2521	0.9441	0.03	−12.2891	0.4857
	NS	6.6	0.898	7.34506	0.03	34.33	0.6926

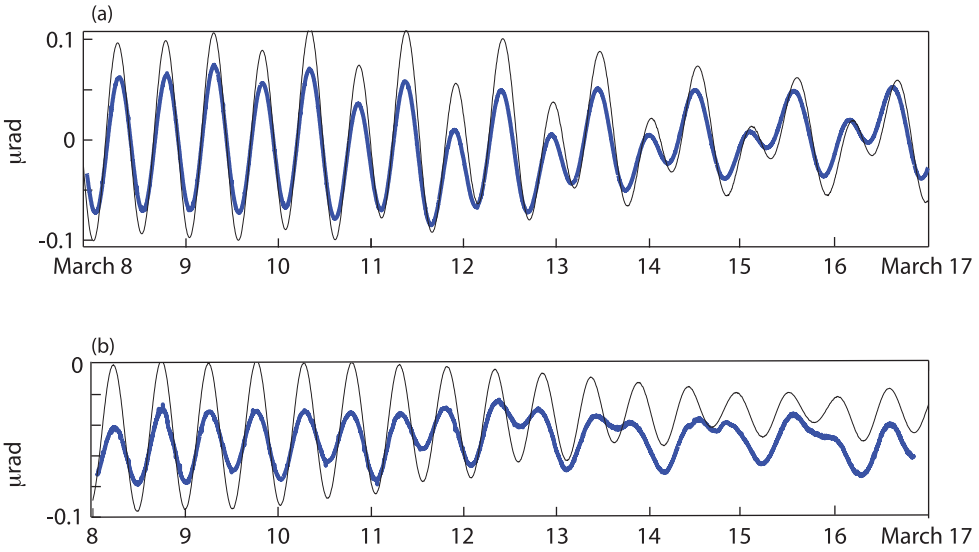

Figure 12. (a) East–west measured tilts (thick blue curve) and solid and oceanic tides prediction (black curve); (b) same as (a) for north–south component

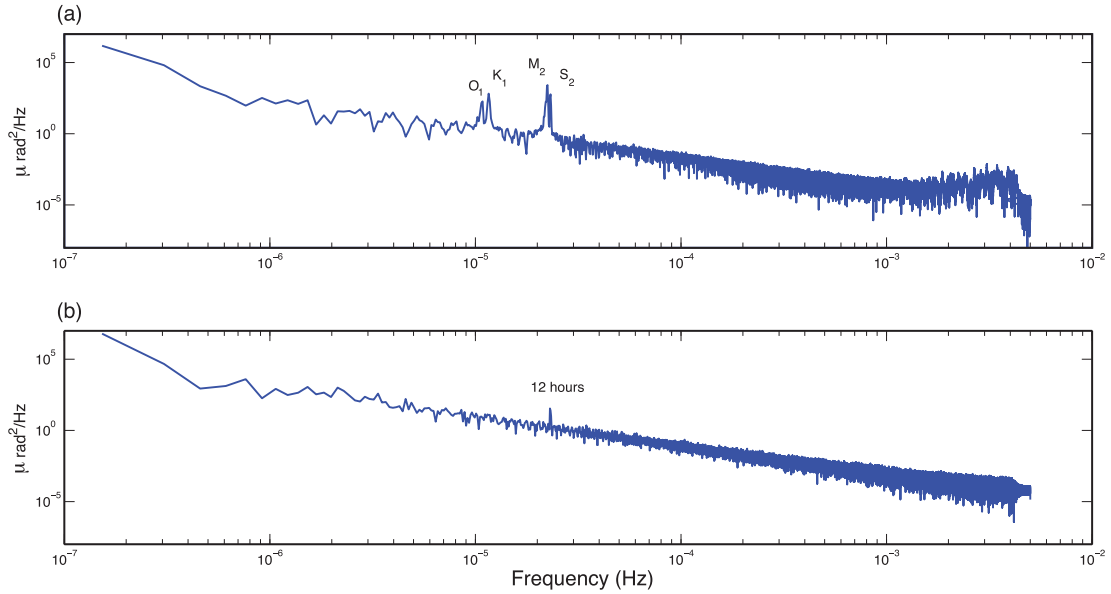

Figure 13. (a) Power spectrum density (PSD) of 4 months of the west–east tilt showing diurnal and semi-diurnal tides components; (b) PSD of 4 months of the common-mode. Solid Earth tides components are completely absent from the common-mode, the slight remaining peak frequency being the signature of atmospheric tides.

8 DISCUSSION AND CONCLUSION

We have described a newly constructed simple pendulum borehole tiltmeter based on an optical interferometric displacement sensor (EFFPI) equipped with long optical fibres. This OBT, with a length of approximately 0.85 m, is designed to allow the tracking of horizontal 2-D movements of a borosilicate bob suspended to a flexible rod. Analysis of the pendulum shows that it displays ground tilts with a resonance frequency of 0.6 Hz and acts as a low-pass filter of the ground acceleration. This OBT further allows for accurate differential measurement due to its three optical axes oriented such that the sum of the three measured displacements theoretically

vanishes. For our practical device, this sum contains distance variations common to the three axes. The critical interest in this differential measurement is to allow a reconstruction of the 2-D displacement of the pendulum bob along the east–west and north–south directions free from all electronic, optical, thermal or atmospheric pressure drifts.

During the first four months of its installation in the low-noise underground laboratory LSBB in Rustrel, France, a quasi-linear drift of 2.50 μm has been observed in the differential measurements, corresponding to a tilt of 3.57 μrad. Because such a drift has not been recorded by a high-stability long baseline tiltmeter installed in the same tunnel, we attribute this apparent tilt to a very slow non-uniform slip of the ring holding the optical collimators. Alternatively, this drift could also be related to the instrument-ground coupling technique or a local deformation of the tunnel housing the instrument (e.g. Harrison 1976). Nevertheless, the measured displacements revealed a highly accurate Earth tide measuring capability and a very good sensitivity to the Earth's normal modes provoked by large earthquakes.

In terms of perspectives, a low-power version of this instrument, useful for many geophysical applications, is under investigation. Also, a completely welded mechanical device should prevent drifts associated with a plastic or viscous internal deformation of the pendulum. Nevertheless, this first version of our OBT has several advantages over previously developed compact tiltmeters:

(1) Long fibres separating the tiltmeter from its electronic driver allow installation of the sensor in boreholes and in deep sea without requiring any source of energy at the measurement point.

(2) This tiltmeter is entirely passive and is expected to have a long functioning time (currently more than 2 yr of continuous operation). The electronic driver at the surface can be easily replaced if required.

(3) The conception of common-mode displacement by a simple sum allows elimination of most environmental and instrumental noises such as pressure, temperature, humidity and laser diode wavelength variations. These corrections are made at nano-radian level.

(4) The sensitivity of the optical tiltmeter to both static tilts and ground motions allows the detection of both sub-surface tilts and seismic waves.

Another major advantage of this tiltmeter lies in that the mechanical, optical and electronic systems consist of relatively cost-effective manufactured parts. For example, costly stabilized Lasers are not required because small wavelength variations are compensated from tilts by correcting from the common-mode displacement. In addition, the current version of the mechanical part of this OBT consists of assembling and integrating relatively inexpensive components such as borosilicate tubes, steel-silica collimators and silica mirrors. Therefore, the cost of the tiltmeter alone is approximately 1500 Euros. The cost of the present version of the complete EFFPI device developed within the OSE Group of the LAAS laboratory is estimated at less than 10 000 Euros. It would thus be potentially feasible to build commercial OBTs at relatively low unit cost for deploying large networks around faults, volcanoes and geological reservoirs.

ACKNOWLEDGEMENTS

This work has been supported by the ANR-RISKNAT (grant number ANR-08-RISKNAT-012–02/LINES) and by the 'Pole de Compétitivité Risques'. The authors would like to thank the technical staff of LSBB-Rustrel for their assistance and advice during the installation and the maintenance of all LINES instruments between 2011 and 2014. We also thank the Editor Duncan Agnew, Walter Zürn and another anonymous reviewer for their thorough reviews.

REFERENCES

Agnew, D.C., 1986. Straimeters and tiltmeters, *Rev. Geophys.*, **24**, 579–624.

Allen, R.V., 1972. A borehole tiltmeter for measurements at tidal sensitivity, *Bull. seism. Soc. Am.*, **62**, 815–821.

Allen, R.V., Wood, D. & Mortensen, C., 1973. Some instruments and techniques for the measurement of tidal tilt, *Phil. Trans. R. Soc. Lond., A.*, **274**, 219–222.

Bernard, P., 2001. From the search of precursors to the research on crustal transients, *Tectonophysics*, **338**, 225–232.

Blevins, D., 2001. *Formulas for Natural Frequency and Mode Shape*, Krieger Pub. Corp., 506 pp.

Boy, J.P., Longuevergne, L., Boudin, F., Jacob, T., Lyard, F., Llubes, M., Florsch, N. & Esnoult, M.F., 2009. Modelling atmospheric and induced non-tidal oceanic loading contributions to surface gravity and tilt measurements, *J. Geodyn.*, **48**, 182–188.

Cattoen, M. & Seat, H.C., 2012. Dispositif à fibre optique extrinsèque pour la mesure d'un paramètre physique, patent application (FR 10 56230, France et WO 2012/013698, International).

Chawah, P., 2012. Développement d'un capteur de déplacement à fibre optique appliqué à l'inclinométrie et à la sismologie, *PhD thesis*, Univ. Montpellier 2, Montpellier, France.

Chawah, P. *et al.*, 2012. Amplitude and phase drift correction of EFPI sensor systems using both adaptive Kalman filter and temperature compensation for nanometric displacement estimation, *IEEE/OSA J. Lightwave Technol.*, **30**, 2195–2202.

Chéry, J. & Collard, P., 2013. Inclinomètre de forage à mesure triaxiale, patent application FR 1251622, France.

Ciddor, P.E., 1996. Refractive index of air: new equations for the visible and near infrared, *Appl. Opt.*, **35**, 1566–1573.

Gaffet, S.Y. *et al.*, 2003. Simultaneous seismic and magnetic measurements in the Low Noise Underground Laboratory (LSBB) of Rustrel, France, during the 2001, 26th January Indian earthquake, *Geophys. J. Int.*, **155**, 981–990.

Harrison, J.C., 1976. Cavity and topographic effects in tilt and strain measurement, *J. geophys. Res.*, **81**, 319–328.

Heydemann, P.L.M., 1981. Determination and correction of quadrature fringe measurement errors in interferometers, *Appl. Opt.*, **20**, 3382–3384.

Hirose, H., 2011. Tilt records prior to the 2011 off the Pacific coast of Tohoku Earthquake, *Earth Planets Space*, **63**, 655–658.

Jahr, T., Letz, H. & Jentzsch, G., 2006. Monitoring fluid induced deformation of the Earth's crust: a large scale experiment at the KTB location/Germany, *J. Geodyn.*, **41**, 190–197.

Kato, M., 1977. Observations of crustal movements by newly-designed horizontal pendulum and water-tube tiltmeters with electromagnetic transducers, *Bull. Disaster Prevent. Res. Inst.*, **27**, 155–171.

King, G.C.P. & Bilham, R.G., 1973. Tidal tilt measurement in Europe, *Nature*, **243**, 74–75.

Kohl, M.L. & Levine, J., 1995. Measurement and interpretation of tidal tilts in a small array, *J. geophys. Res.*, **100**(B3), 3929–3941.

Kümpel, H.J., Lehmann, K., Fabian, M. & Mentes, G., 2001. Point stability at shallow depths: experience from tilt measurements in the Lower Rhine Embayment, Germany, and implications for high-resolutions GPS and gravity recordings, *Geophys. J. Int.*, **146**, 699–713.

Meertens, C.M. & Wahr, J.M., 1986. Topographic effect on tilt, strain, and displacement measurements, *J. geophys. Res.*, **91**(B14), 14 057–14 062.

Mortensen, C.E. & Johnston, M.J.S., 1975. Nature of surface tilt along 85 km of San Andreas fault: preliminary results from a 14-instrument array, *Pure appl. Geophys.*, **113**, 237–249.

Pozar, T. & Mozina, J., 2011. Enhanced ellipse fitting in a two-detector homodyne quadrature laser interferometer, *Meas. Sci. Technol.*, **22**, 085301.

Rosenbach, O. & Jacoby, H., 1969. First experience with the Askania borehole tiltmeter (Earth tide pendulum), in *Problems of Recent Crustal Movements: Third International Symposium*, pp. 467–478, Moscow, U.S.S.R. Academy of Science.

Sakata, S. & Sato, H., 1986. Borehole-type tiltmeter and three-component strainmeter for earthquake prediction, *J. Phys. Earth*, **34**, 129–140

Schwartz, S.Y. & Rokosk, J.M., 2007. Slow slip events and seismic tremor at circum-pacific subduction zones, *Rev. Geophys.*, **45**(3), August 2007, RG3004, doi:10.1029/2006RG000208.

Seat, H.C. *et al.*, 2012. Dual-modulation fiber Fabry-Perot interferometer with double reflection for slowly-varying displacements, *Optics Lett.*, **37**, 2886–2888.

Skalsky, L. & Picha, J., 1969. On some problems of tidal observations with tiltmeters and their accuracy, *Studia geoph. et geod.*, **13**, 138–172.

Spiegel, M.R., 1972. *Théorie et application de la mécanique générale*, chapter II, SerieSchaum, pp. 282–310.

Weise, A., Jentzsch, G., Kiviniemi, A. & Kääriäinen, J., 1999. Comparaison of long-period tilt measurements: results from the two clinometric stations Metsähovi and Lohja, Finland, *J. Geodyn.*, **27**, 237–256.

Welch, P.D., 1967. The use of fast fourier transform for the estimation of power spectra: a method based on time averaging over short, modified periodograms, *IEEE Trans. Audio Electroacoust.*, **AU-15**, 70–73.

Wenzel, H.-G., 1996. The nanogal software: Earth tide data processing package ETERNA 3.30, *Bulletin d'Informations Marées Terrestres*, **124**, 9425–9439.

Wiener, N., 1949. *Extrapolation, Interpolation and Smoothing of Stationary Time Series With Engineering Applications*, The MIT Press.

Wu, S., Fan, S., Luo, J. & Hsu, H., 2002. Folded pendulum tiltmeter, *Rev. Sci. Instrum.*, **87**, 2150–2156.

Wyatt, F. & Berger, J., 1980. Investigations of tilt measurements using shallow borehole tiltmeters, *J. geophys. Res.*, **85**, 4351–4362.

Wyatt, F.K., Morrissey, S.-T. & Agnew, D.C., 1988. Shallow borehole tilt—a reprise, *J. geophys. Res.*, **93**, 9197–9201.

Zumberge, M.A., Berger, J., Dzieciuch, M.A. & Parker, R.L., 2004. Resolving quadrature fringes in real time, *Appl. Optics*, **43**, 771–775.

APPENDIX A

Lagrange's equations are a powerful analytical tool for calculating the motion equations of a system. Although it is derived from Newton's laws, Lagrange formalism has a number of inherent advantages. It uses scalar quantities rather than vectors, hence its shape is independent of the coordinates used. If we consider the LINESOBT as a conservative system where the forces are derived from a potential E_p, the kinetic energy E_c can be related to E_p by the following Lagrange equation (Spiegel 1972).

$$\frac{d}{dt}\left(\frac{\partial \mathcal{L}}{\partial \dot{\Theta}}\right) - \frac{\partial \mathcal{L}}{\partial \Theta} = 0 \tag{A1}$$

in which

$$\mathcal{L} = Ec - Ep \tag{A2}$$

is the Lagrangian and Θ the pendulum rotation relative to the reference coordinates. Solving the instrument's motion equation then enables the calculation of the potential and kinetic energies of the system.

Potential energy associated with the bending of the rod

When the frame undergoes a very slow or quasi-static tilt of angle Λ, the junction P moves accordingly while the stable state of the pendulum follows the local vertical. Since P is a flexible hinge, a slight bending appears on the rod. A restoring moment caused by the stiffness of the rod appears on the hinge and tends to compensate the bending moment. This creates a resisting force whose normal is $||\vec{F}_r|| = \frac{3EJ_G}{L^2}\Theta = \frac{k_r}{L}\Theta$, with E Young's modulus, J_G the quadratic moment of the section over the hinge, L being the length of the rod and k_r the equivalent spiral spring stiffness. The resulting potential energy associated with the bending of the rod is then:

$$E_{p_r} = \frac{1}{2}k_r\Theta^2. \tag{A3}$$

Potential energy associated with the gravity

The borosilicate rod has a mass that may be non-negligible. The bob at the end of the rod is cylindrical and contains mirrors that reduce the density of the bob. The problem then simplifies to a pendulum formed by a bob coupled to a flexible rod. To calculate the potential energy associated with the weight and the kinetic energy of the system, we let ℓ be the distance from the centre of rotation P to the centre of inertia of the pendulum and by R the radius of gyration.

When the centre of mass undergoes an elementary movement, the elementary work provided by the force of gravity is written as $dW_P = -Mgl\sin(\Lambda+\Theta)\,d\Theta$, with Λ being the frame tilt relative to the Cartesian coordinate system. Thus, the potential energy associated with the weight of the pendulum opposes the work done and is written as:

$$E_{p_p} = -Mgl\cos(\Lambda+\Theta) + constant \tag{A4}$$

$$Ep = E_{p_r} + E_{p_p}. \tag{A5}$$

Kinetic energy

Initially, let the essentially moving frame be fixed (see Fig. 2). In this case, the kinetic energy of the oscillations is limited to:

$$E_c = \frac{1}{2}J_P\dot{\Theta}^2 = \frac{1}{2}MR^2\dot{\Theta}^2. \tag{A6}$$

Nevertheless, in the reference $(O, \vec{I}, \vec{J}, \vec{K})$, $(P, \vec{i}, \vec{j}, \vec{k})$ undergoes a rotation of angle Λ and translations $(\vec{X}_P, \vec{Y}_P, \vec{Z}_P)$. The total kinetic energy finally becomes:

$$E_c = \frac{1}{2}M\left\{\begin{array}{c}\dot{X}_Q^2(t) + \dot{Z}_Q^2(t) + R^2(\dot{\Lambda}+\dot{\Theta})^2 + \\ 2R(\dot{\Lambda}+\dot{\Theta})[\dot{X}_P(t)\cos(\Lambda+\Theta) + \dot{Z}_P(t)\sin(\Lambda+\Theta)]\end{array}\right\}. \tag{A7}$$

Friction force

Now, during the oscillation of the pendulum, the latter is subject to air resistance force that opposes its speed. In these conditions, the system is now more-realistically considered as non-conservative and the modified Lagrange equation becomes:

$$\frac{\mathrm{d}}{\mathrm{d}t}\left(\frac{\partial \mathcal{L}}{\partial \dot{\Theta}}\right) - \frac{\partial \mathcal{L}}{\partial \Theta} = F_f, \tag{A8}$$

where $F_f = -k_f L\dot{\Theta}$ is the frictional force and k_f the coefficient of friction. Using eqs (A4) and (A6), the generic eq. (A8) can be developed into:

$$\ddot{\Theta}(t) + \frac{k_f l}{MR^2}\dot{\Theta}(t) + \frac{\mathrm{gl}}{R^2}\left(1 + \frac{k_r}{Mgl}\right)\Theta(t) = -\ddot{\Lambda}(t) - \frac{\mathrm{gl}}{R^2}\Lambda(t) - \frac{1}{R}\ddot{X}_P(t) \tag{A9}$$

with M the mass of the pendulum, R the radius of gyration, l the distance from the rotation centre P to the pendulum's inertial centre, g the gravitational acceleration, Λ the frame tilt relative to the inertia space and $\ddot{X}_Q$ the frame acceleration relative to the coordinate system. A more compact form of equilibrium is given by:

$$\ddot{\Theta}(t) + 2\xi\Omega_0\dot{\Theta}(t) + \Omega_0^2\Theta(t) = -\ddot{\Lambda}(t) - \Omega_1^2\Lambda(t) - \frac{1}{R}\ddot{X}_P(t) \tag{A10}$$

with ξ a damping ratio, Ω_0 the angular frequency associated with rod bending (the frequency then being $f_0 = {}^{\Omega_0}/_{2\pi}$) and Ω_1 the ideal natural angular frequency. We experimentally found a value of 0.02 for ξ. According to equation (A10), the rotation $\Theta(t)$ of the pendulum is then influenced by the tilt $\Lambda(t)$ of the frame and also by its translational movement $X_P(t)$.

APPENDIX B

The frequency response of our instrument shows that the pendulum reacts in its primary mode of oscillations as a low pass filter of the frame's acceleration, but encounters an amplification at its proper frequency (blue curve of Fig. B1). One solution to fight against this resonance problem would be to mechanically damp the vibrations (by immersing the instrument in a viscous fluid as example). While effective, this solution should greatly attenuate the signal on a large frequency band. We use a signal processing method whose principle is to convolute the pendulum movement with an equalizer filter in order to create a virtual damping precisely on the resonant frequency of the pendulum. A model of this ideal instrument response looks like the cyan curve in Fig. B1.

A statistical approach to minimize the error between a desired model and the output of a filter in the presence of a stationary noise was proposed by Norbert Wiener (Wiener 1949, see Fig. B2). The equations of Wiener-Hopf are used to calculate the coefficients of the impulse response of an equalizer filter $H_e\left(q^{-1}\right)$ (red curve in Fig. B1) which, convoluted with the pendulum response $H_p\left(q^{-1}\right)$ (blue curve in Fig. B1), gives the desired function $H_m\left(q^{-1}\right)$. The output of the equalizer filter represents the movement of the numerically damped pendulum.

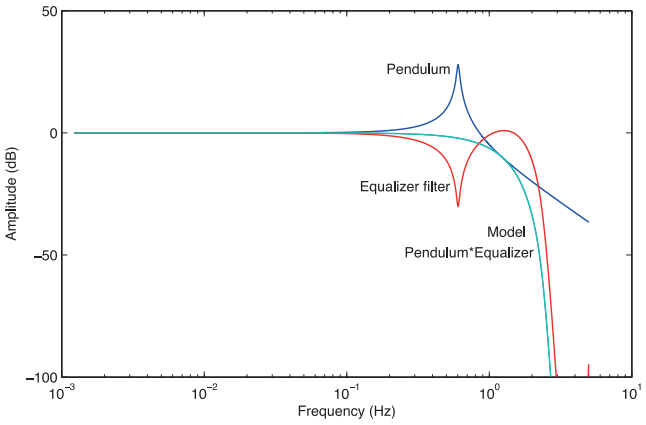

Figure B1. Virtual damping of the pendulum motion using a Wiener equalizer filter. Blue curve: raw response of the instrument. Red curve: equalizer filter calculated by solving the Wiener-Hopf equations. Cyan curve: response of the equalized pendulum. Green curve (superimposed to cyan curve): response of the ideal model.

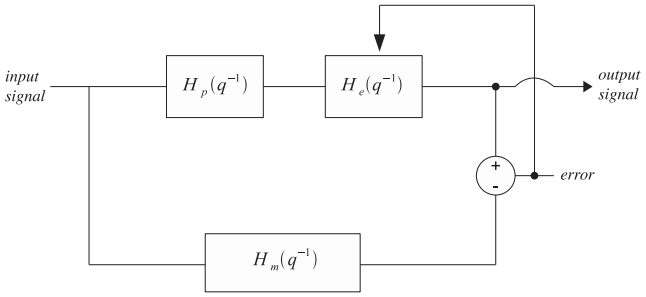

Figure B2. Principle of the equalizer filter used to artificially increase the damping coefficient of the pendulum. The mechanical filter of the pendulum $H_p\left(q^{-1}\right)$ is convoluted with the equalizer filter $H_e\left(q^{-1}\right)$ to create a function equivalent to a low-pass model filter $H_m\left(q^{-1}\right)$ without resonance, q being the q-transform operator or the time advance in a discrete time signal.